Dynamics of the O-Atom Exchange Reaction $^{16}O(^3P) + {}^{18}O{}^{18}O(^3\Sigma_g^-) \rightarrow {}^{16}O{}^{18}O(^3\Sigma_g^-) + {}^{18}O(^3P)$ at Hyperthermal Energies

Sridhar A. Lahankar, Jianming Zhang, and Timothy K. Minton*

Department of Chemistry and Biochemistry, Montana State University

Bozeman, MT 59717, USA

Hua Guo

Department of Chemistry and Chemical Biology, University of New Mexico

Albuquerque, NM 87131, USA

György Lendvay*

Institute of Materials and Environmental Chemistry, Research Centre for Natural Sciences,

Hungarian Academy of Sciences

P.O. Box 286, H-1525 Budapest, Hungary

* Authors to whom correspondence should be addressed. Electronic mail: tminton@montana.edu, lendvay.gyorgy@ttk.mta.hu.

ABSTRACT

The O-atom exchange reaction, $^{16}O(^3P) + {}^{18}O^{18}O(^3\Sigma_g^-) \rightarrow {}^{16}O^{18}O(^3\Sigma_g^-) + {}^{18}O(^3P)$, was investigated at a hyperthermal center-of-mass (c.m.) collision energy (E_{coll}) of 86 kcal mol^{-1}, using a crossed-molecular-beams apparatus and quasi-classical trajectory (QCT) calculations. The inelastically scattered ^{16}O and reactively scattered $^{16}O^{18}O$ products were detected with a rotatable mass spectrometer employing electron-impact ionization. The ^{16}O atoms are scattered in inelastic collisions in the forward direction relative to their initial direction of flight, with most of the available energy partitioned into translation ($\langle E_T \rangle$ = 90%). The $^{16}O^{18}O$ products of reactive collisions are mainly formed through impulsive dynamics and are scattered in the forward as well as sideways directions relative to the direction of the reagent ^{16}O atoms, with a slight majority of the available energy partitioned into translation ($\langle E_T \rangle$ = 58%) and a significant contribution to internal degrees of freedom. Excellent agreement was found between the experimental c.m. angular and translational energy distributions of the inelastically scattered ^{16}O and reactively scattered $^{16}O^{18}O$ products and those obtained from QCT calculations, which were carried out on a ground-state singlet electronic potential energy surface. The QCT calculations predicted $^{16}O^{18}O$ products that are both highly rotationally and vibrationally excited, with $j'(^{16}O^{18}O)$ up to 150 and $v'(^{16}O^{18}O)$ up to 15, respectively. The QCT simulations indicate that the translational energy distribution of the reactively scattered $^{16}O^{18}O$ is bimodal, corresponding to two distinct interaction mechanisms that are dependent on impact parameter: one at impact parameters below ~0.5 Å and another in the vicinity of 1.6 Å. Collisions in the former regime produce $^{16}O^{18}O$ with internal energy closer to the maximum available energy while the latter mechanism, involving strong interaction within the O_3 potential well, is responsible for the low-energy peak of the product translational distribution. The inelastic collisions also follow two

basic impact-parameter-dependent mechanisms. At impact parameters above 2.1 Å, the ^{16}O atom is reflected from the outer repulsive wall of the O_2 molecule, resulting in exclusively forward scattering, while collisions at impact parameters below ~2 Å access the O_3 potential well and lead to ejection of either an ^{16}O or an ^{18}O atom. Scattering remains preferentially forward in both cases due to the large momentum of the attacking ^{16}O atom.

I. INTRODUCTION

The O-atom exchange reaction $O'(^3P) + O_2(^3\Sigma_g^-) \rightarrow O'O(^3\Sigma_g^-) + O(^3P)$ has attracted special interest because of its importance in atmospheric chemistry and the curious isotope effect it exhibits.[1, 2] This reaction occurs in Earth's atmosphere and competes with ozone formation. The kinetics of ozone formation and depletion are well documented in the ozone-oxygen cycle, also known as Chapman mechanism.[3] This cycle begins with collisions of atomic and molecular oxygen to form metastable ozone (O_3), which can be stabilized after transfer of its excess energy to a third partner. Ozone absorbs ultraviolet light from the Sun and photodissociates with the involvement of multiple electronic potential energy surfaces (PESs) to re-form atomic and molecular oxygen.[4-7] Very interesting isotope effects have been reported in ozone chemistry.[8, 9] Several groups have reported unusual enrichment of heavy ozone, $^{50}O_3$, in stratospheric ozone samples.[10-12] _ENREF_13_ENREF_16 Numerous explanations for the unexpected enrichment have been offered in the literature since then. Isotope-dependent rates of ozone formation and the competing atom exchange reactions have been measured,[13-16] and the small change in reaction exoergicity due to the difference in zero-point energies of different isotopologues was proposed as a possible explanation for the unexpected isotope enrichment. However, zero-point energy effects may not be sufficient to alter ozone kinetics significantly,[16] leading to the conclusion that

the isotope effect is dynamically driven.[17-21] It seems clear that the dynamics of both the bimolecular step and the collisional stabilization of the transient O_3 complex are important.[22]

The lack of detailed dynamical data on the bimolecular O-atom exchange reaction motivated joint experimental and theoretical investigations of the reaction,

$$^{18}O(^3P) + {}^{16}O^{16}O(^3\Sigma_g^-) \rightarrow {}^{16}O^{18}O(^3\Sigma_g^-) + {}^{16}O(^3P), \qquad (1)$$

which were carried out at center-of-mass (c.m.) collision energies of E_{coll} = 5.7 and 7.3 kcal mol^{-1}.[1, 2] The c.m. angular and translational energy distributions of $^{16}O^{18}O$ products were derived from crossed-molecular-beams experimental results. The angular distribution showed forward-backward symmetry with slight preference for scattering in the forward direction relative to the direction of the incoming reagent ^{18}O atoms. The total c.m. translational energy distribution showed a maximum close to the available energy (E_{avl}), suggesting relatively little rotational and vibrational excitation in the products. The rotational distribution of product $^{16}O^{18}O$ was determined to be non-statistical. Quantum statistical (QS) and quasi-classical trajectory (QCT) calculations were carried out by Van Wyngarden *et al.*[1, 2] on the ground-state PES developed by Babikov *et al.*,[23] based on the earlier work of Siebert, Schinke, and Bittererova.[24] This PES for the O + O_2 system is characterized by a deep well corresponding to O_3, with a submerged potential barrier ("reef") in the O + O_2 entrance/exit channel, now thought to be an artifact.[25-27] If the complex lived long enough, then the energy would be completely randomized among the degrees of freedom, and the products would be scattered into all spatial directions with equal probability, corresponding to a forward-backward symmetric c.m. angular distribution. The QS model, assuming complete randomization of the energy in the complex, produced exactly such a distribution. However, the slight forward-scattering bias for the O-atom exchange product observed in the experiments indicated that the energy is not completely randomized in the

collision complex. The QCT calculations, handling the dynamics explicitly, capture the forward bias of the experiments, but the calculations predict a stronger forward bias than what was observed.[1, 2] Nevertheless, both the experiment and QCT calculations provided direct evidence that the O-atom exchange dynamics are not statistical. This non-statistical nature of the reaction was further confirmed by recent quantum scattering calculations.[9,21]

While the previous studies of O-atom exchange in O + O_2 collisions have relevance to thermally equilibrated processes in the atmosphere, there are also situations in the natural atmosphere and in induced environments where highly non-equilibrium conditions may lead to O + O_2 collisions at hyperthermal collision energies of tens of kcal mol^{-1}. The source of O atoms in the natural atmosphere is photodissociation of O_2 and O_3 by solar ultraviolet light, which may lead to very fast O atoms and subsequent collisions at hyperthermal velocities. For example, O(^3P) may be formed with velocities as high as 6 km s^{-1},[28, 29] corresponding to E_{coll} ~ 46 kcal mol^{-1}. Hyperthermal O + O_2 collisions can also occur in the shock layer of a hypersonic vehicle,[30-32] where temperatures may be many thousands of degrees Kelvin and a small fraction of collisions may therefore occur with relative velocities greater than 6 km s^{-1}. In addition, the high temperature and velocity exhaust gas of an air-breathing hypersonic vehicle, such as a scramjet,[33, 34] may allow for O + O_2 collisions at hyperthermal collision energies. In hypersonic flow environments, both inelastic energy transfer and O-atom exchange reactions are important in models of energy exchange that aim to predict the structure of the shock wave. The high energies associated with collisions of O with O_2 under extreme conditions have the potential to alter the dynamics substantially and lead to a large non-statistical disposal of energy into the products. At hyperthermal collision energies, any higher energy barriers that might prevent entrance into the O_3 potential well from certain directions could be surmounted, leading to

reaction at collision geometries that would be forbidden or improbable at lower energies and subsequent angular distributions and energy disposal into product degrees of freedom that would not easily be predictable. In addition, high collision energies could shift the balance between inelastic and reactive (O-atom exchange) collisions, thus affecting the internal state distributions of the O_2 products.

The dynamics of hyperthermal inelastic or reactive collisions may, in principle, be affected by the involvement of multiple PESs; thus, the potential challenge for theory in describing hyperthermal collision dynamics is high. Nevertheless, it has been found for the hyperthermal atom-exchange reactions that have been studied to date ($O + C^{18}O$,[35] $O + C^{18}O_2$,[36] $O + H_2O$,[37] and $O_2 + C^{18}O_2$[38]) that calculations on a ground-state PES were in good agreement with the results of crossed-molecular-beams studies, leading to the conclusion that the hyperthermal collision dynamics for these systems are dominated by a ground-state PES. The $O + O_2$ system might therefore also be well characterized by a ground-state PES. Even if the ground-state O_3 PES does control the dynamics at hyperthermal collision energies, it is also unclear *a priori* how its potential energy well may influence the dynamics at these energies. By extending the experimental and theoretical study of $O + O_2$ collisions to hyperthermal energies, the details of the dynamics of this system that are relevant to extreme natural and induced environments can be revealed, and the validity of a PES in current use may be tested for its relevance in such environments.

We have conducted a joint experimental crossed-molecular-beams and theoretical QCT investigation, on a ground-state PES, that considers both inelastic and reactive collisions of $^{16}O(^3P)$ with $^{18}O^{18}O(^3\Sigma_g^-)$ at a hyperthermal collision energy. The experiment can distinguish between the inelastic and reactive channels through the detection of ^{16}O and $^{16}O^{18}O$, respectively,

and has provided differential cross sections for these channels that are not resolved by the internal state of O_2. The QCT calculations agree well with the experiment and address the state-to-state cross sections for the inelastic scattering interaction,

$$^{16}O(^3P) + {}^{18}O^{18}O(^3\Sigma_g^-, v = 0, j) \rightarrow {}^{16}O + {}^{18}O^{18}O(^3\Sigma_g^-, v', j'), \quad (2)$$

and the O-atom exchange reaction,

$$^{16}O(^3P) + {}^{18}O^{18}O(^3\Sigma_g^-, v = 0, j) \rightarrow {}^{18}O + {}^{16}O^{18}O(^3\Sigma_g^-, v', j'). \quad (3)$$

The inelastic scattering dynamics are reported here for the first time, for any collision energy, and the dynamics of the O-atom exchange reaction differ substantially from what was observed for relatively low-energy collisions of O amd O_2. The QCT calculations predict the experimental results well, suggesting that the ground-state PES that was used is sufficient for describing the dynamics of hyperthermal $O + O_2$ collisions.

II. EXPERIMENTAL METHODS

The experiments were performed with the use of a crossed-molecular-beams apparatus equipped with a rotatable mass spectrometer detector and a hyperthermal atomic-oxygen beam source. The details of the apparatus and molecular beam source have been described earlier.[39] A pulsed, hyperthermal atomic-oxygen beam was crossed at right angles with a pulsed, supersonic beam of $^{18}O^{18}O$ gas (Sigma Aldrich, 99%). Both beams operated at a repetition rate of 2 Hz.

The hyperthermal atomic-oxygen beam was produced with a laser-detonation source employing a piezoelectric pulsed valve of our own design. Molecular oxygen at a pressure of 500 psig was used as the precursor gas. At a delay set in the range 170-190 μs after the triggering of the pulsed valve, a ~7.0 J pulse^{-1} CO_2 TEA laser was fired. The IR laser light at

10.6 μm passed through an antireflection coated ZnSe window into the source chamber where it was focused into the nozzle using a bare gold mirror of 1 m radius of curvature. The concentrated laser pulse initiated a breakdown of the gas and heated the resulting plasma to more than 40,000 K. The detonation wave dissociated and accelerated the oxygen gas in the conical nozzle (10 cm long, 20° included angle). The resulting beam pulse contained both atomic and molecular oxygen, traveling at hyperthermal velocities in the range ~6−9 km s^{-1}. The hyperthermal beam pulse followed a doubly differentially pumped path that started at the apex of the conical nozzle and then passed through two apertures at 83.5 cm (10 mm diameter) and 89.5 cm (2 mm diameter) before reaching the main scattering chamber. A relatively narrow range of velocities was selected from the overall beam pulse with the use of a synchronized, 17.8-cm-diameter chopper wheel rotating at 300 Hz. The chopper wheel had three slots, 1.5 mm wide, and was placed just past the 2 mm diameter aperture. The velocity-selected hyperthermal beam crossed the supersonic beam at 95.2 cm from the nozzle apex. The nominal velocity of the O-atom beam used to study the $^{16}O(^3P)$ reaction with $^{18}O^{18}O$ was 8026 m s^{-1}, corresponding to a c.m. collision energy of E_{coll} = 86 kcal mol^{-1}. The full width at half maximum (FWHM) of the O-atom beam velocity was ~587 m s^{-1}, corresponding to a c.m. collision energy width of 12 kcal mol^{-1}. The mole fraction of atomic oxygen in the beam was approximately 80 percent, with the balance being O_2.

The pulsed beam of pure $^{18}O^{18}O$ was created by using a second piezoelectric pulsed valve, with a nozzle diameter of 1.0 mm. The stagnation pressure was 1500 Torr. The pulsed beam started at the nozzle, traveled 3 cm and passed through a 5-mm-diameter skimmer into a differential pumping region, then traveled 2.5 cm more before passing through a 2.5-mm-diameter aperture into the main scattering chamber (held at ~10^{-7} Torr). From the aperture, the beam

traveled 1.5 cm to the crossing point of the two beams. The distance from the nozzle to the crossed-beams interaction region was therefore 7 cm. The nominal $^{18}O^{18}O$ beam velocity was estimated to be ~694 m s^{-1}. The velocity of the $^{18}O^{18}O$ beam was about 1/12 that of the O-atom beam, and the beam velocity width was therefore very narrow compared to that of O-atom beam. Thus the velocity width of the $^{18}O^{18}O$ beam was not considered in the analysis.

Scattered products went through an electron-impact ionizer,[40] which was 33.7 cm from the nominal crossing point of the two beams. The ionized products were mass-selected by a quadrupole mass filter and then counted by a Daly-type ion counter.[41] Number density distributions, *N(t)*, of scattered products were accumulated as a function of their arrival time with a multi-channel scaler. These number density distributions, which are commonly called time-of-flight (TOF) distributions, were collected at different detector angles and were integrated to give laboratory angular distributions $N(\Theta)$. The laboratory angle, Θ, is the detection direction with respect to the hyperthermal O-atom beam, where 0° is aligned with the O-atom beam and 90° is aligned with the $^{18}O^{18}O$ beam. Figure 1a shows a Newton diagram for inelastic scattering (purple) and O-atom exchange (blue) with all available energy portioned into translation, with E_{coll} = 86 kcal mol^{-1}. The laboratory frame angular detection range used in the experiment is also shown. The c.m. collision energy distribution is shown in Figure 1b. A forward convolution method was used to derive a c.m. translational energy distribution, $P(E_T)$, and a c.m. angular distribution, $T(\theta)$, from the laboratory TOF and angular distributions.[39]

TOF distributions of $^{16}O^{18}O$ reaction products were collected at a mass-to-charge ratio (m/z) of 34 ($^{16}O^{18}O^+$); TOF distributions of inelastically scattered ^{16}O atoms were detected at m/z = 16 ($^{16}O^+$). These distributions were collected in 2° increments from Θ = 6° to 24° and in 3° increments from Θ = 24° to 48°, respectively.

III. THEORETICAL METHODS

Calculations were carried out on an electronic ground-state PES developed by Babikov *et al*.[23] and another by Dawes *et al*.,[26] using the standard quasiclassical trajectory (QCT) method for both reactive and nonreactive collisions, with the Gaussian weighting method and the standard histogram technique for reference. State-to-state quantum dynamics at such high collision energies are still too difficult. Details of QCT calculations are reported in Refs. [2, 42-44] _ENREF_25 The parameters specific to the calculations presented here are as follows. The collision energy was set at 86 kcal mol^{-1} (3.73 eV) or was selected randomly from a Gaussian distribution centered at the same energy with a width parameter of 6 kcal mol^{-1}, corresponding to the spread in the experimental c.m. collision energies. The initial and final separations were both 12 Å, and the maximum impact parameter was 4.0 Å. The vibrational quantum number of the reactant O_2 was $v = 0$, and its rotational quantum number was set to one of $j = 1$, 11, or 21. In the final-state analysis, the Gaussian width parameter was 0.05. For a detailed description see Ref. [43]. For each set of initial states, 8,000,000 trajectories were calculated on the Babikov *et al*. PES[23] and 20,000 on the Dawes *et al*. PES.[25, 26] The inelastic and reactive translational energy and angular distributions calculated on the two PESs were identical within statistical error. This agreement suggests that, as expected, because of the very large collision energy, the presence or absence of the submerged reef in the $O + O_2$ channel, which is the main difference between the two PESs, does not significantly influence the dynamics of the collisions. In this paper, we report the distributions obtained on the Babikov *et al.*[23] PES because of the much better statistics.

IV. RESULTS

A. Inelastic Collisions. In the experiments, the lab frame TOF and angular distributions of the inelastically scattered ^{16}O atoms were measured. In the QCT calculations, a collision was considered inelastic if the rotational or the vibrational quantum number of the $^{18}O^{18}O$ molecule changed by one (note that in classical mechanics the "quantum number" associated with the angular momentum of the molecule changes continuously and that we have disregarded the symmetry restrictions on the final rotational states). Figures 2a-c show representative lab-frame TOF distributions, and Figure 2d shows the lab-frame angular distribution, along with the best-fit curves derived from the c.m translational energy, $P(E_T)$, and angular, $T(\theta)$, distributions shown in Figures. 3a,b and the lab-frame predictions from the QCT c.m. translational energy and angular distributions, also shown in Figs 3a,b. As seen in Fig. 2, both sets of $P(E_T)$ and $T(\theta)$ distributions in Fig. 3 (red and blue) give good fits to the lab-frame TOF and angular distributions. The experimental and QCT $P(E_T)$ and $T(\theta)$ distributions show the same trends, but their widths differ. The fact that the lab-frame predictions, calculated from the best-fit experimental and the QCT c.m. $P(E_T)$ and $T(\theta)$ distributions through the forward convolution method, are almost identical is an indication that the forward convolution procedure is not very sensitive to the exact shape of the c.m. distributions. This insensitivity is understandable in part because, when the $P(E_T)$ and $T(\theta)$ distributions are fairly narrow, the width of the lab-frame TOF distributions is dominated by the temporal width of the incident hyperthermal beam pulse, which is ~20 μs FWHM. There are additional broadening effects, from the distribution of c.m. collision energies in the experiment,

the uncertainty in flight path from the finite sizes of the crossing regions of the two beams and the ionization volume of the electron-impact ionizer, and the finite angular spread of detection angles. While we attempt to account for all the broadening effects in our analysis, errors cannot be avoided especially when the $P(E_T)$ and $T(\theta)$ distributions of the relevant dynamical process are very narrow. When deriving c.m. distributions from the experimental TOF and angular distributions, we typically make the $P(E_T)$ distribution as broad as possible such that it still gives a good fit to the TOF data. This standard procedure leads to a best-fit $P(E_T)$ distribution whose width is roughly an upper limit. Thus, the width of the "true" or "canonical" $P(E_T)$ distribution may be smaller. If the $P(E_T)$ distribution is too broad, then the c.m. angular distribution is likely to have to be made too narrow in order to give an acceptable fit to the lab-frame angular distribution. Indeed, the QCT calculations give a $P(E_T)$ distribution that is narrower than the best-fit experimentally-derived $P(E_T)$ distribution, and they give a $T(\theta)$ distribution that is broader than the experimentally-derived $T(\theta)$ distribution. A test was done to approximate the broadening effects in the experiment by running a set of QCT calculations with a Gaussian distribution of collision energies that matched the experimental distribution, and it was found that the QCT $P(E_T)$ distribution became broader and was close to the shape of the experimental best-fit $P(E_T)$ distribution. This test was a further indication of the good agreement between the experimental and QCT results. Having thus gained a fair degree of confidence in the QCT calculations, we chose to focus on a single collision energy (86 kcal mol^{-1}) and use the QCT results for this energy to characterize the inelastic scattering dynamics. The $T(\theta)$ distribution obtained from QCT calculations is characterized by a forward peak that decays by a factor of 10 within 30 degrees (Fig. 3a). The nearly-elastic peak of the calculated final translational energy distribution is very narrow, with FWHM < 2 kcal mol^{-1}. This distribution for $O(^3P)$ + $^{18}O^{18}O$ is

much narrower than the $P(E_T)$ distribution observed in inelastic scattering during hyperthermal collisions of a system that might be expected to have similar dynamical behavior, $O(^3P) + C^{18}O$, where the FWHM is >10 kcal mol^{-1}.[35]

B. Reactive Collisions: Isotope Exchange. Representative TOF and angular distributions of reactively scattered product $^{16}O^{18}O$ molecules in the laboratory frame are shown in Figs. 4a-d and Fig. 4e, respectively. The $P(E_T)$ and $T(\theta)$ distributions used to obtain these fits are shown in Fig. 5. The $T(\theta)$ distribution in Fig. 5a indicates that the $^{16}O^{18}O$ product is forward and sideways scattered with respect to the direction of the reagent ^{16}O atom. The $P(E_T)$ distribution in Fig. 5b has a maximum at 55 kcal mol^{-1}, with an average of $\langle E_T \rangle$ = 49.8 kcal mol^{-1}, which is 58% of the available energy (E_{avl} = 86 kcal mol^{-1}). Thus, a significant amount of energy (on average 36 kcal mol^{-1}) goes into internal excitation of the $^{16}O^{18}O$ product.

Figures 6a-c show vibrationally and rotationally resolved distributions of reactively scattered $^{16}O^{18}O(v',j')$ molecules, obtained from the QCT calculations. For comparison, the analogous QCT results for inelastic scattering are also shown in Figs. 6d-e. For all product vibrational states, the newly formed $^{16}O^{18}O$ molecules are mostly forward scattered relative to the direction of the reagent ^{16}O atoms (Fig. 6a). The overall c.m. translational energy distribution (Fig. 6b) has an average energy of 52.7 kcal mol^{-1}, which corresponds to an average internal excitation of 33.3 kcal mol^{-1}, or ~8 vibrational quanta. For low vibrational states (up to $v' = 4$) of the product $^{16}O^{18}O$ molecules, the translational energy distributions are bimodal, with one peak near the available energy and one peak at about 30 kcal mol^{-1} lower energy. The presence of a low-translational-energy peak when $v' \leq 4$ and the relatively high probabilities of forming $^{16}O^{18}O$ products in these vibrational states indicate that a significant fraction of reactive collisions produce rotationally hot $^{16}O^{18}O$ molecules. The presence of the

low-translational-energy peak makes the overall translational energy distribution very broad and gives rise to maximum at a relatively low E_T. Figure 6c shows the vibrationally resolved rotational distribution for the $^{16}O^{18}O$ product. The peak in the rotational distribution near $j' = 90$ for $v' = 0 - 4$ corresponds to the lower energy bump in the translational energy distribution at about 50 kcal mol^{-1} (Fig. 6b). As the vibrational excitation increases, the peak of the rotational distribution shifts toward lower quantum numbers, and its height reduces because the available energy decreases. Accordingly, the low-translational-energy peak (Fig. 6b) becomes less pronounced.

In comparison with reactive collisions, the location of the peak of the rotational distribution of the $^{18}O^{18}O$ molecules after inelastic collisions is at about $j' = 50$ for low product vibrational excitation and varies slightly with the vibrational quantum number (Fig. 6f). The shape of this distribution hardly depends on whether the initial rotational quantum number is 1 or 11. For collisions in which the vibrational quantum number of $^{18}O^{18}O$ remains 0, the peak of the rotational distribution is orders of magnitude higher than for $v' \neq 0$ and is located at $j' = 2$ and $j' = 12$, respectively, for initial $j = 1$ and $j = 11$.

In test calculations, the product state distributions at $E_{coll} = 86$ kcal mol^{-1} were found to be identical within statistical error for mass combinations 16-18-18, 18-18-18, and 16-16-16. This allows us to make an estimate of the combined final vibrational and rotational state distribution of the O_2 molecule after collisions with an O atom, approximately valid for all three mass combinations, including both reactive and inelastic collisions. The tabulated data for the 16-16-16 combination, which dominates $O + O_2$ collisions in the atmosphere, can be found in Table S1 of the supporting information.

V. DISCUSSION

We have observed markedly different dynamics for inelastic collisions and isotope exchange reactions, even though both channels are apparently governed by the same ground-state PES.

The $P(E_T)$ distribution for inelastic scattering from QCT calculations in Figure 3b is very narrow and has a maximum only slightly below the available energy of 86 kcal mol^{-1}, indicating that after the collision $^{18}O^{18}O$ is generally vibrationally unexcited and has a low level of rotational excitation. The $P(E_T)$ distribution thus indicates that mildly rotationally inelastic collisions dominate the inelastic scattering dynamics, and the $T(\theta)$ distribution (Fig. 3a) shows that ^{16}O atoms are preferentially scattered in the forward direction, relative to the direction of the reagent ^{16}O atoms, leading to the conclusion that they are produced in large-impact-parameter collisions.

As described in section IV B, a broad $P(E_T)$ distribution is required to fit the experimental data for the isotope exchange reaction, implying that the $^{16}O^{18}O$ product has a broad distribution of internal energies. The experimental $P(E_T)$ distribution, seen in Fig. 5, ranges from 10 to 86 kcal mol^{-1} and has a maximum at ~56 kcal mol^{-1}. However, the distribution is fairly flat between 40 and 60 kcal mol^{-1} and the width is large (FWHM ~ 65 kcal mol^{-1}). The $P(E_T)$ distribution from the QCT calculations is also broad, and it agrees well with the experimental $P(E_T)$ distribution on the high-energy wing. But at lower translational energies it runs significantly below the latter, the deviation being the largest near 30 kcal mol^{-1}. This difference is believed to be outside the error range of the experiment and suggests that the QCT calculations may underestimate the extent of highly internally excited $^{16}O^{18}O$ products, similar to what was reported in the studies done with lower collision energies.[1,2]

The most surprising feature of the QCT product translational energy distribution for isotope exchange is the bimodality of the vibrationally resolved $P(E_T)$ distributions, which hints at a dual mechanism for the O-atom exchange reaction (see Fig. 6b). In the analogous distributions for inelastic collisions there are also signs of a second peak but it is hardly visible because it is superimposed on the tail of the narrow quasi-elastic peak. In order to understand this possible dual mechanism, we have run 1,000,000 trajectories at fixed impact parameters, b, set at 0.1 Å intervals from 0 to 4.0 Å. The opacity functions for both the reactive and inelastic processes are shown in Fig. 7. The probability of O-atom exchange is below 20% at zero impact parameter and increases to about 30% at b = 1.5 Å, and it decays quickly as b increases further. The probability of inelastic energy transfer (defined as collisions resulting in excitation of $^{18}O^{18}O$ by at least one rotational or vibrational quantum) complements that of the reaction to unity up to b = 2.1 Å. At larger impact parameters, the probability of inelastic collisions decreases (with elastic collisions dominating) because the interaction is weak.

Concerning the dynamics of the energy transfer and O-atom exchange, the fraction of collisions in which the system enters the potential well is informative. During integration of each trajectory, we recorded the lowest potential energy. Trajectories during which the potential energy went lower than –0.4 kcal mol^{-1} are considered to have entered the potential well. Figure 7 also shows the probability of such collisions, separated according to inelastic and reactive collisions and their sum. In the vast majority of collisions with impact parameters above 2 Å, which are essentially all inelastic, the interaction energy remains repulsive during the entire encounter, and in the small fraction of these high-impact-parameter inelastic collisions where the trajectory visits the attractive part of the PES, the potential energy does not decrease below about –0.4 kcal mol^{-1}. This indicates that the mechanism of inelastic energy transfer is different in the

large and small impact parameter domains. In the former, not surprisingly, the glancing encounters are favorable for pure rotational excitation of the (initially cold) O_2 molecule, while in the latter, there is very strong interaction between the partners, and both rotational and vibrational excitation may occur.

The mechanism of O-atom exchange at very small impact parameters is especially interesting. As can be seen in Fig. 7, the sum of the probabilities for entering the potential well in reactive and inelastic encounters remains below unity for all impact parameters, suggesting that some collisions do not enter the potential well even when the impact parameter is very low. Indeed, as Fig. 7 indicates, when $b < 0.5$ Å about one half of reactive events take place without entering the potential well. Although this may seem surprising, the inspection of animated trajectories provides an explanation (see Supporting Information for examples of animated trajectories). In collisions of this type, the attacking O atom approaches almost perpendicular to the axis of the O_2 molecule, but always somewhat closer to one of its ends. Then it hits the closer O atom from which it is repelled towards the other, going through an almost equilateral triangular configuration, and then it departs with the O atom that was farther away at the point of initial encounter. In most of the reactive collisions with impact parameters larger than ~0.5 Å, the attacking O atom enters the well and forms a bond with one of the two ^{18}O atoms. Remarkably, there are also encounters in this impact parameter domain in which pure vibrational energy transfer takes place. In such events the arrangement of the three atoms remains close to collinear throughout the collision.

Another special case is the mechanism of O-atom exchange in the vicinity of the peak of the opacity function, at $b \sim 1.6$ Å. This impact parameter is favorable for entering the potential well without changing the course of the attacking atom, so the system goes deep into the

potential well. The section of the PES in Fig. 8 shows that at this impact parameter the cone of acceptance is very large, but in order to enter the well without any barrier the ^{16}O atom has to arrive at an angle to the axis of the $^{18}O^{18}O$ molecule and there will be a torque that causes the complex to start to rotate as a whole, generating a rotationally excited (reactive or nonreactive) product. The arrows in Fig. 8 illustrate two limiting cases. If the attacking ^{16}O atom enters the potential well in the direction towards the center of the molecule, it hits the repulsive wall marked by B in Fig. 8, from which it will be repelled without O-atom exchange, inducing rotational and vibrational excitation of the reactant molecule. On the other hand, if the direction of approach points toward one of the ^{18}O atoms, the attacking ^{16}O hits the repulsive wall marked by A in Fig. 8. Such trajectories may lead to reaction if the ^{18}O–^{18}O stretch vibration is in the expanding phase. The ^{16}O will then pull the attacked ^{18}O farther away from the other and abstract it with a large probability. The nascent $^{16}O^{18}O$ product will consequently be highly rotationally excited because of the initial sideways component of the relative momentum.

If the three atoms formed a long-lived complex, one would expect complete mixing of energy and a product distribution that is both statistical in its dynamical behavior and its distribution of reactive vs. inelastic products. At low collision energies, the lifetime of a fraction of collisions has been found to be long enough to achieve statistical distribution of reactive vs. inelastic products,[1,2] i.e., the three O atoms leave the complex with equal probability, yielding a branching ratio 2:1 for reactive vs. non-reactive decomposition of the complex. However, even at collision energies as low as 5.7 kcal mol^{-1}, the angular distribution of the reactively scattered products shows forward bias. At the high collision energy of our study, the forward bias is much more intense. In fact, our calculations have shown that with the increase of the collision energy the forward biased angular distributions retain a remarkable turn-up at 180°, which

disappears only at a high collision energy of ~66 kcal mol^{-1}. Animated trajectories at E_{coll} = 86 kcal mol^{-1} show that in the majority of collisions the three O atoms spend only one or two stretch vibration periods together, and the visual impression is similar to trajectories of direct reactions. Even though in almost all collisions at impact parameters below 2.1 Å the system does enter the potential well, the time spent as a three-atom complex is far too short for energy randomization and the collision dynamics are effectively impulsive. Even if the three-atom complex lived longer, it would not be expected to achieve complete randomization of energy because of the relatively shallow potential well and the highly harmonic nature of the PES immediately below the dissociation limit.[24, 45] It is thus not surprising that the maximum probability of reaction in Fig. 7 is only about 30%.

The dynamical picture outlined above is supported by two-dimensional plots of distributions (Figs. 9a-d) that show how the reaction or inelastic collision probability varies with impact parameter and scattering angle or final translational energy. Figures 9a and 9b show 2D plots of the angular distribution at various impact parameters for inelastically and reactively scattered products, respectively. The vast majority of inelastic collisions (Fig. 9a) take place at large impact parameters and correspond to forward scattering. Fig. 9a also shows a peak at small impact parameters. In fact, only a small fraction (~ 4%) of collisions takes place at $b < 0.4$ Å. Among them, inelastic collisions scatter the attacking atom backward, and reactive collisions also tend to scatter the product ($^{16}O^{18}O$) into the sideways or backward direction (Fig. 9b). These peaks are not visible in the calculated overall (and similarly the experimentally observable) angular distribution, which is an average over all impact parameters, where the low impact parameter range has a low weight. As a result, the effect of the collisions at low impact parameters is not evident. Among inelastic collisions, those occurring at large impact parameters

are almost elastic, where the energy converted from translation to rotation is predominantly one or two rotational quanta (Fig. 9c). More energy goes to rotation and vibration of the inelastically scattered O_2 at impact parameters slightly below 2 Å and also when the impact parameter is very small. About one half of inelastic trajectories in the former region and all of them at small *b* (see Fig. 7) enter the potential well where strong interaction between the degrees of freedom takes place.

The main feature in the angular distribution for reactive $^{16}O^{18}O$ products is also preferential forward scattering, which is seen in the QCT and experimental results. Collisions responsible for forward scattering occur at medium impact parameters, between ~1.0 and 1.8 Å (Fig. 9b). In this impact parameter range the distribution extends to relatively large scattering angles because, as mentioned above, the system penetrates the potential well, and because this situation occurs with bent O-O-O arrangements. This impact parameter range is responsible for the breadth of the experimental angular distribution. Figure 9d shows that the impact parameter region of 1.0 to 1.8 Å has an exceptional role in determining the shape of the reactive $P(E_T)$ distribution, too (Fig. 9d). The large width of the experimental translational energy distribution comes from this range of impact parameters, where the O-atom exchange probability is also the largest (see Fig. 7). In the low-impact-parameter regime ($b < 0.5$ Å), the peak of the translational energy distribution is at 65 to 83 kcal mol^{-1}, slightly decreasing when *b* increases. The same pattern can be seen in Fig. 9c, which indicates that in this impact parameter range the internal motion in the encounter complex is similar and it is more or less a question of chance whether the outcome is reactive or inelastic.

The dependencies of the probability of formation of reactive or inelastic products in particular rotational and vibrational states with impact parameter (Fig. S1, Supporting Information) are consistent with those of the translational energy and angular distributions and show that the impact parameter range between about 1.0 and 1.8 Å is where large rotational and large vibrational

energy transfer takes place not only in the collisions leading to O-atom exchange but also to inelastic energy transfer.

The QCT calculations were performed on a ground-state PES and produced results in good agreement with the experiment. At the very large collision energy in our system, excited electronic states are energetically available. The fact that the dynamics calculations reproduce the experiments very well and provide a sensible explanation for the observed features suggests, in the spirit of Occam's razor, that there is no need to assume that the excited electronic states are involved in the dynamics. This can be rationalized by considering that the very large velocities of atoms that occur in our study are not favorable for nonadiabatic transitions. However, even when higher electronic states are not involved, nonadiabatic dynamics may occur in ground-state reactions as a result of fine-structure effects, which was observed in the $O + D_2 \rightarrow OD + D$ reaction.[46, 47] Nevertheless, in this example, the rovibrational state distributions were predicted well with theoretical calculations that did not consider these additional effects. Thus, we cautiously suggest that a ground-state PES should be sufficient in situations where the goal is to explain the nuclear dynamics in $O + O_2$ collisions up to hyperthermal energies.

VI. CONCLUSION

A combined crossed molecular beams and quasiclassical trajectory (QCT) study has been performed to understand the outcome of $^{16}O(^3P) + {}^{18}O{}^{18}O(^3\Sigma_g^-)$ collisions at a hyperthermal collision energy of 86 kcal mol.$^{-1}$ The QCT calculations relied only on a ground-state PES to describe the dynamics, and the results of these calculations agreed well with the experimental observations. The experimentally observed translational energy and angular distributions have some remarkable characteristics. The translational energy distribution for the products of O-

atom exchange is broad, and the angular distribution of the reactively scattered $^{16}O^{18}O$ is also broad. While it is strongly forward biased, the fraction of sideways and backward scattered products is significant, reflecting a complex interaction between the ^{16}O atom and the $^{18}O^{18}O$ molecule that leads to O-atom exchange. On the other hand, the translational energy distributions for the inelastically scattered products and the angular distribution of the inelastically scattered ^{16}O are exceedingly narrow, indicative of scattering that is dominated by high-impact-parameter collisions.

The QCT calculations reveal three qualitatively different interaction mechanisms that depend on impact parameter. In the large impact parameter range above 2.1 Å, collisions are inelastic or even elastic. The translational energy distribution corresponding to products of these collisions consists of a very narrow nearly elastic peak. For such collisions, the colliding partners do not enter deep into the potential well. Collisions are glancing, and the attacking atom is forward scattered. In the intermediate impact parameter range between 1.0 and 1.8 Å, the system enters the potential well in essentially all collisions. In both reactive and inelastic encounters, the products are preferentially forward scattered, but significant sideways scattering can be seen if a large amount of the available energy is transferred into rotation and/or vibration. The attacking atom remains in close contact with the other two O atoms for one or two stretch vibrational periods, and the attacking atom (^{16}O) is preferentially ejected. For the collisions in which the partners do react, significant rotational excitation and sideways scattering can be seen, because the attacking atom enters the potential well at an angle to the axis of the O_2 molecule. Collisions in this intermediate impact parameter range are responsible for the large width of the experimental translational energy distribution and the relatively large sideways and backward scattering in O-atom exchange encounters. In the low-impact parameter range (<1.0 Å), most

collisions enter the potential well and are repelled by the inner wall. In inelastic collisions, the ^{16}O atom is scattered backward. In reactive collisions, sideways and backward scattering dominate. In less than 10% of such collisions, the system does not enter the potential well. All such collisions are reactive and instantaneous. The attacking O atom first hits one of the atoms of the molecule and then forms a bond with the other with which it departs.

Even though the system enters the potential well in the most reactive intermediate impact parameter range, the attacking atom departs alone in more than 65% of the cases because the collision energy is so large that the complexes are not long-lived. The effect is not because of the small mass difference between the attacking ^{16}O atom and the ^{18}O atoms of the molecule. According to the QCT calculations, in which nuclear statistics are not taken into account, all distributions remain, within Monte Carlo error, the same when the attacking atom's mass is changed to ^{18}O. The deviation from non-statistical dynamical behavior due to the short-lived complexes is similar to but much more extreme than the behavior observed at lower collision energies.[1, 2]

The cross sections for O-atom exchange and energy transfer are 3.0 and 22.0 $Å^2$ according to the QCT calculations. The ratio of these is 1:7.3. From the experiment we obtained 1:5.25 for the same ratio, which is in reasonably good agreement. The cross section for the transfer of one or more vibrational quanta is also very large, around 6 $Å^2$. The average internal energy in the O_2 molecule after the collision is about 12 kcal mol^{-1} or 14% of the initial collision energy, one half of which comes from O-atom exchange and one half from inelastic collisions. Thus, in extreme environments where O and O_2 may collide with hyperthermal relative velocities, the scattered O_2 molecules will be highly vibrationally and rotationally excited. The use of a

ground-state PES to describe the energy disposal in these hyperthermal inelastic and reactive collisions should be appropriate.

ASSOCIATED CONTENT

Supporting Information. Table of vibrationally resolved rotational distributions for the $^{32}O_2$ molecule after ^{16}O + $^{16}O^{16}O$ collisions. Probability density plots showing the correlation between impact parameter and vibrational and rotational distributions for inelastic and reactive collisions.

This material is available free of charge via the Internet at http://pubs.acs.org.

ACKNOWLEDGMENTS

This work has been supported by the U.S. Air Force Office of Scientific Research, Grant No. FA9550-10-1-0563 (TKM), the Hungarian Scientific Research Fund, Grant No. K108996 (GL), the Hungarian National Development Agency, Grant No. KTIA_AIK_12-1-2012-0014 (GL), and The United States Department of Energy, Grant No. DE-FG02-05ER15694 (HG).

REFERENCES

1. Van Wyngarden, A. L.; Mar, K. A.; Boering, K. A.; Lin, J. J.; Lee, Y. T.; Lin, S.-Y.; Guo, H.; Lendvay, G., Nonstatistical behavior of reactive scattering in the $^{18}O+^{32}O_2$ isotope exchange reaction, *J. Am. Chem. Soc.* **2007,** *129*, 2866-2870.
2. Van Wyngarden, A. L.; Mar, K. A.; Quach, J.; Nguyen, A. P. Q.; Wiegel, A. A.; Lin, S.-Y.; Lendvay, G.; Guo, H.; Lin, J. J.; Lee, Y. T., et al., The non-statistical dynamics of the $^{18}O + ^{32}O_2$ isotope exchange reaction at two energies, *J. Chem. Phys.* **2014,** *141*, 064311.
3. Chapman, S., Ozone and atomic oxygen in the upper atmosphere, *Philos. Mag.* **1930,** *10*, 369-383.
4. Grebenshchikov, S. Y.; Qu, Z. W.; Zhu, H.; Schinke, R., New theoretical investigations of the photodissociation of ozone in the Hartley, Huggins, Chappuis, and Wulf bands, *Phys. Chem. Chem. Phys.* **2007,** *9*, 2044-2064.

5. Schinke, R.; Grebenshchikov, S. Y., On the photodissociation of ozone in the range of 5-9 eV, *Chem. Phys.* **2008,** *347*, 279-287.
6. Schinke, R.; McBane, G. C.; Shen, L.; Singh, P. C.; Suits, A. G., Production of O_2 Herzberg states in the deep UV photodissociation of ozone, *J. Chem. Phys.* **2009,** *131*, 011101.
7. Grebenshchikov, S. Y.; Rosenwaks, S., Ab initio quantum mechanical study of the $O(^1D)$ formation in the photolysis of ozone between 300 and 330 nm, *J. Phys. Chem. A* **2010,** *114*, 9809-9819.
8. Schinke, R.; Grebenshchikov, S. Y.; Ivanov, M. V.; Fleurat-Lessard, P., Dynamical studies of the ozone isotope effect: A status report, *Annu. Rev. Phys. Chem.* **2006,** *57*, 625-661.
9. Sun, Z.; Liu, L.; Lin, S. Y.; Schinke, R.; Guo, H.; Zhang, D. H., State-to-state quantum dynamics of O + O_2 isotope exchange reactions reveals non-statistical behavior at atmospheric conditions, *Proc. Natl. Acad. Sci. USA* **2010,** *107*, 555-558.
10. Thiemens, M. H.; Heidenreich III, J. E., The mass-independent fractionation of oxygen: A novel isotope effect and its possible cosmochemical implications, *Science* **1983,** *219*, 1073-1075.
11. Irion, F. W.; Gunson, M. R.; Rinsland, C. P.; Yung, Y. L.; Abrams, M. C.; Chang, A. Y.; Goldman, A., Heavy ozone enrichments from ATMOS infrared solar spectra, *Geophys. Res. Lett.* **1996,** *23*, 2377-2380.
12. Mauersberger, K.; Lämmerzahl, P.; Krankowsky, D., Stratospheric ozone isotope enrichments—Revisited, *Geophys. Res. Lett.* **2001,** *28*, 3155-3158.
13. Mauersberger, K.; Erbacher, B.; Krankowsky, D.; Gunther, J.; Nickel, R., Ozone isotope enrichment: isotopomer-specific rate coefficients, *Science* **1999,** *283*, 370-372.
14. Janssen, C.; Guenther, J.; Krankowsky, D.; Mauersberger, K., Relative formation rates of $^{50}O_3$ and $^{52}O_3$ in ^{16}O-^{18}O mixtures, *J. Chem. Phys.* **1999,** *111*, 7179-7182.
15. Janssen, C.; Guenther, J.; Krankowsky, D.; Mauersberger, K., Erratum to Relative formation rates of $^{50}O_3$ and $^{52}O_3$ in ^{16}O-^{18}O mixtures, *J. Chem. Phys.* **2000,** *112*, 11109.
16. Janssen, C.; Guenther, J.; Mauersberger, K.; Krankowski, D., Kinetic origin of the ozone isotope effect : a critical analysis of enrichments and rate coefficients, *Phys. Chem. Chem. Phys.* **2001,** *3*, 4718-4721.
17. Fleurat-Lessard, P.; Grebenshchikov, S. Y.; Schinke, R.; Janssen, C.; Krankowsky, D., Isotope dependence of the O + O_2 exchange reaction: Experiment and theory, *J. Chem. Phys.* **2003,** *119*, 4700-4712.
18. Fleurat-Lessard, P.; Grebenshchikov, S. Y.; Siebert, R.; Schinke, R.; Halberstadt, N., Theoretical investigation of the temperature dependence of the O + O_2 exchange reaction, *J. Chem. Phys.* **2003,** *118*, 610-621.
19. Schinke, R.; Fleurat-Lessard, P.; Grebenshchikov, S. Y., Isotope dependence of the lifetime of ozone complexes formed in O + O_2 collisions, *Phys. Chem. Chem. Phys.* **2003,** *5*, 1966-1969.
20. Schinke, R.; Fleurat-Lessard, P., The effect of zero-point energy differences on the isotope dependence of the formation of ozone: a classical trajectory study, *J. Chem. Phys.* **2005,** *122*, 094317.
21. Sun, Z.; Yu, D.; Xie, W.; Hou, J.; Dawes, R.; Guo, H., Kinetic isotope effect of the ^{16}O + $^{36}O_2$ and ^{18}O + $^{32}O_2$ isotope exchange reactions: Dominant role of reactive resonances

revealed by an accurate time-dependent quantum wavepacket study, *J. Chem. Phys.* **2015,** *142*, 174312.
22. Ivanov, M. V.; Babikov, D., Mixed quantum-classical theory for the collisional energy transfer and the rovibrational energy flow: Application to ozone stabilization, *J. Chem. Phys.* **2011,** *134*, 144107.
23. Babikov, D.; Kendrick, B. K.; Walker, R. B.; Pack, R. T.; Fleurat-Lesard, P.; Schinke, R., Metastable states of ozone calculated on an accurate potential energy surface, *J. Chem. Phys.* **2003,** *118*, 6298-6308.
24. Siebert, R.; Schinke, R.; Bittererova, M., Spectroscopy of ozone at the dissociation threshold: Quantum calculations of bound and resonances states on a new global potential energy surface, *Phys. Chem. Chem. Phys.* **2001,** *3*, 1795-1798.
25. Dawes, R.; Lolur, P.; Ma, J.; Guo, H., Communication: Highly accurate ozone formation potential and implications for kinetics, *J. Chem. Phys.* **2011,** *135*, 081102.
26. Dawes, R.; Lolur, P.; Li, A.; Jiang, B.; Guo, H., Communication: An accurate global potential energy surface for the ground electronic state of ozone, *J. Chem. Phys.* **2013,** *139*, 201103.
27. Tyuterev, V. G.; Kochanov, R.; Campargue, A.; Kassi, S.; Mondelain, D.; Barbe, A.; Starikova, E.; De Backer, M. R.; Szalay, P. G.; Tashkun, S., Does the "reef structure" at the ozone transition state towards the dissociation exist? New insight from calculations and ultrasensitive spectroscopy experiments, *Phys. Rev. Lett.* **2014,** *113*, 143002.
28. Stranges, D.; Yang, X.; Chesko, J. D.; Suits, A. G., Photodissociation of ozone at 193 nm by high-resolution photofragment translational spectroscopy, *J. Chem. Phys.* **1995,** *102*, 6067-6077.
29. Matsumi, Y.; Kawasaki, M., Photolysis of atmospheric ozone in the ultraviolet region, *Chem. Rev.* **2003,** *103*, 4767-4781.
30. Anderson, J. D., Hypersonic and High Temperature Gas Dynamics, *(American Instititute of Aeronautics and Astronautics, Reston, VA, 1989) Chapter 9*.
31. Andrienko, D.; Boyd, I. D., Investigation of oxygen vibrational relaxation by quasi-classical trajectory method, *Chem. Phys.* **2015,** *459*, 1-13.
32. Andrienko, D. A.; Boyd, I. D., High fidelity modeling of thermal relaxation and dissociation of oxygen, *Physics of Fluids* **2015,** *27*, 116101.
33. Hidding, B.; Pfitzner, M.; Simone, D.; Bruno, C., Review of the potential of silanes as rocket/scramjet fuels, *Acta Astronautica* **2008,** *63*, 379-388.
34. Kang, S. H.; Yang, S. S.; Lee, Y. J., Using various types of ground tests various types of ground tests, *Combust. Sci. Technol.* **2012,** *184*, 1553-1567.
35. Brunsvold, A. L.; Upadhyaya, H. P.; Zhang, J.; Cooper, R.; Minton, T. K.; Braunstein, M.; Duff, J. W., Dynamics of hyperthermal collisions of $O(^3P)$ with CO, *J. Phys. Chem. A* **2008,** *112*, 2192-2205.
36. Yeung, L. Y.; Okumura, M.; Zhang, J.; Minton, T. K.; Paci, J. T.; Karton, A.; Martin, J. M. L.; Camden, J. P.; Schatz, G. C., $O(^3P) + CO_2$ collisions at hyperthermal energies: Dynamics of nonreactive scattering, oxygen isotope exchange, and oxygen-atom abstraction, *J. Phys. Chem. A* **2012,** *116*, 64-84.
37. Braunstein, M.; Conforti, P. F., O-atom exchange in $O(^3P) + H_2O(^1A_1)$ collisions, *Chem. Phys. Lett.* **2012,** *523*, 34-38.

38. Yeung, L. Y.; Okumura, M.; Paci, J. T.; Schatz, G. C.; Zhang, J.; Minton, T. K., Hyperthermal O-atom exchange reaction $O_2 + CO_2$ through a CO_4 intermediate, *J. Am. Chem. Soc.* **2009,** *131*, 13940-13942.
39. Garton, D., J.; Brunsvold, A., L.; Minton, T., K.; Troya, D.; Maiti, B.; Schatz, G., C., Experimental and theoretical investigations of the inelastic and reactive scattering dynamics of $O(^3P) + D_2$, *J. Phys. Chem. A* **2006,** *110*, 1327-1341.
40. Brink, G. O., Electron bombardment molecular beam detector, *Rev. Sci. Instrum.* **1966,** *37*, 857-860.
41. Daly, N. R., Scintillation-type mass spectrometer ion detector, *Rev. Sci. Instrum.* **1960,** *31*, 264-267.
42. Lendvay, G.; Xie, D.; Guo, H., Mechanistic insights into the $H + O_2 \rightarrow OH + O$ reaction from quasi-classical trajectory studies on a new ab initio potential energy surface, *Chem. Phys.* **2008,** *349*, 181-187.
43. Bencsura, Á.; Lendvay, G., Bimolecular reactions of vibrationally excited molecules. Roaming atom mechanism at low kinetic energies, *J. Phys. Chem. A* **2012,** *116*, 4445-4456.
44. Szabó, P.; Lendvay, G., Dynamics of complex-forming bimolecular reactions: A comparative theoretical study of the reactions of H atoms with $O_2(^3\Sigma_g^-)$ and $O_2(^1\Delta_g)$, *J. Phys. Chem. A* **2015,** *119*, 12485-12497.
45. Ndengué, S.; Dawes, R.; Wang, X.-G.; Carrington, T.; Sun, Z.; Guo, H., Calculated vibrational states of ozone up to dissociation, *J. Chem. Phys.* **2016,** *144*, 074302.
46. Lahankar, S. A.; Zhang, J.; McKendrick, K. G.; Minton, T. K., Product-state-resolved dynamics of the elementary reaction of atomic oxygen with molecular hydrogen, $O(^3P) + D_2 \rightarrow OD(X^2\Pi) + D$, *Nat. Chem.* **2013,** *5*, 315-319.
47. Lahankar, S. A.; Zhang, J.; Minton, T. K.; McKendrick, K. G., Complete state-resolved non-adiabatic dynamics of the $O(^3P) + D_2 \rightarrow OD(X^2\Pi) + D$ reaction, *J. Am. Chem. Soc.* **2014,** *136*, 12371-12384.

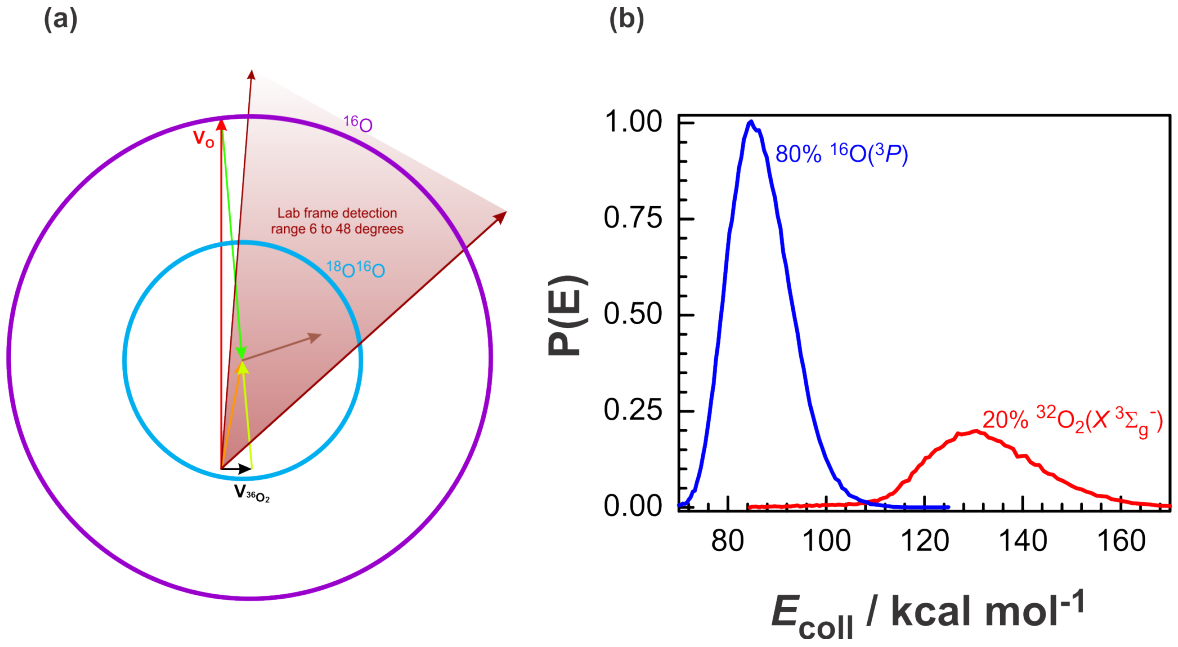

Figure 1. (a) Newton diagram showing the inelastic scattering Newton circle for atomic oxygen (purple) and the reactive scattering Newton circle for the isotope (O-atom) exchange product (blue), assuming that 100% of the available energy goes into translation. (b) Center-of-mass collision energy distributions for ^{16}O-$^{36}O_2$ and $^{32}O_2$-$^{36}O_2$ collisions between the components of the hyperthermal beam and the $^{36}O_2$ in the supersonic beam. The average velocity of the $^{16}O(^3P)$ in the hyperthermal beam was 8037 m s^{-1}, corresponding to a collision energy of 86 kcal mol^{-1} for ^{16}O-$^{36}O_2$ collisions.

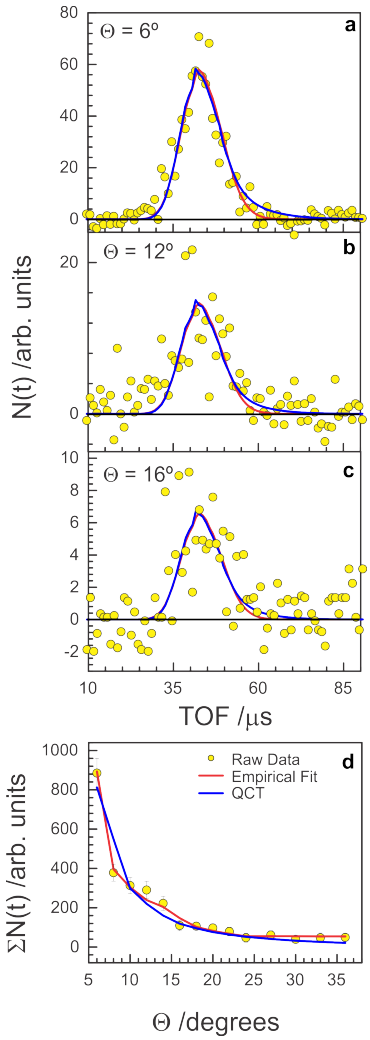

Figure 2. (a-c) Representative time-of-flight distributions and (d) laboratory angular distribution of inelastically scattered $^{16}O(^3P)$ atoms following collisions of $^{16}O(^3P)$ with $^{18}O^{18}O$ at E_{coll} = 86 kcal mol^{-1}. The yellow circles are the experimental data. The solid lines are the forward convolution simulations to the data. The red curves are considered to be the best-fit curves from the experimental data, using the c.m. translational energy and angular distributions shown as red curves in Figs. 3a,b. The blue curves are derived from the QCT c.m. translational energy and angular energy distributions shown as blue curves in Figs. 3a,b. In (d), the error bars represent ±1σ uncertainty in the integrated number density.

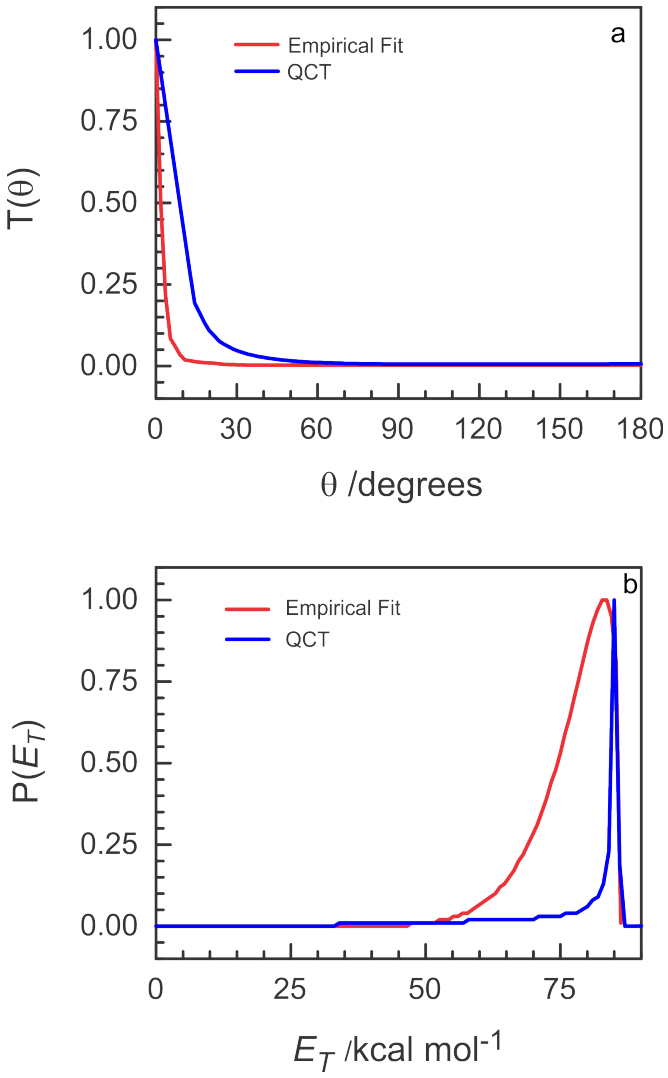

Figure 3. (a) Center-of-mass angular distributions, *T(θ)*, for the inelastically scattered ^{16}O atoms from collisions of $^{16}O(^3P)$ with $^{18}O^{18}O$ at E_{coll} = 86 kcal mol^{-1}. (b) Center-of-mass translational energy distributions, $P(E_T)$, for the inelastically scattered ^{16}O atoms from collisions of $^{16}O(^3P)$ with $^{18}O^{18}O$ at E_{coll} = 86 kcal mol^{-1}. The red curves are considered to be the best-fit distributions from the experiment, and the blue curves come from the QCT calculations.

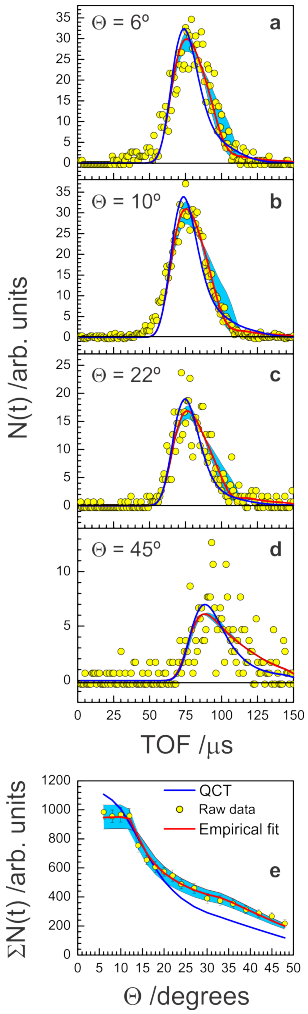

Figure 4. (a-d) Representative time-of-flight distributions and (e) laboratory angular distribution of reactively scattered $^{16}O^{18}O$ molecules following the isotope (O-atom) exchange reaction of $^{16}O(^3P)$ with $^{18}O^{18}O$ at E_{coll} = 86 kcal mol^{-1}. The yellow circles are the experimental data. The red curves are considered to be the best-fit curves from the experimental data, using the c.m. translational energy and angular distributions shown as red curves in Figs. 5a,b. The blue curves are derived from the QCT c.m. translational energy and angular distributions shown as blue curves in Figs. 5a,b. The light-blue shaded regions represent the error in the fit, corresponding to the light-blue shaded regions in Fig. 5. The error bars in (e) represent ±1σ uncertainty in the integrated number density.

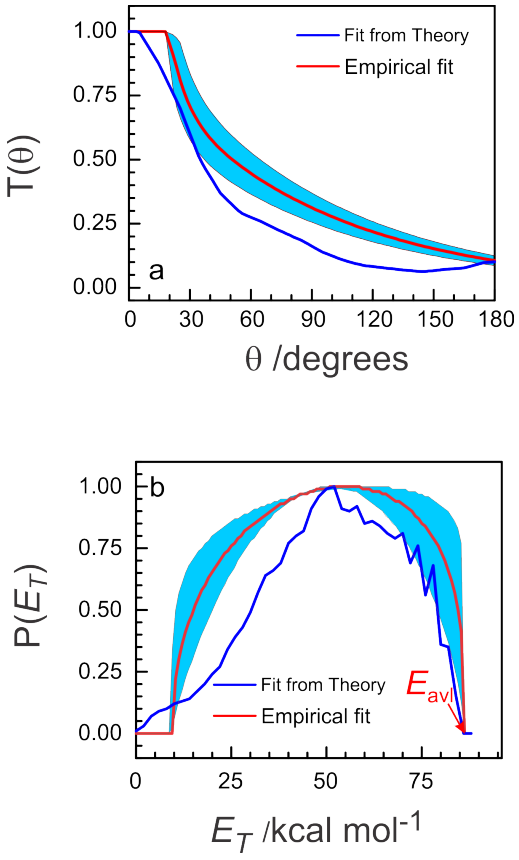

Figure 5. (a) Center-of-mass angular distributions, $T(\theta)$, for reactively scattered $^{16}O^{18}O$ molecules from collisions of $^{16}O(^3P)$ with $^{18}O^{18}O$ at E_{coll} = 86 kcal mol^{-1}. (b) Center-of-mass translational energy distributions, $P(E_T)$, for reactively scattered $^{16}O^{18}O$ molecules from collisions of $^{16}O(^3P)$ with $^{18}O^{18}O$ at E_{coll} = 86 kcal mol^{-1}. The red curves are considered to be the best-fit distributions from the experiment, and the blue curves come from the QCT calculations. The light-blue shaded regions represent the error in the experimental result, corresponding to the light-blue shaded regions in Fig. 4.

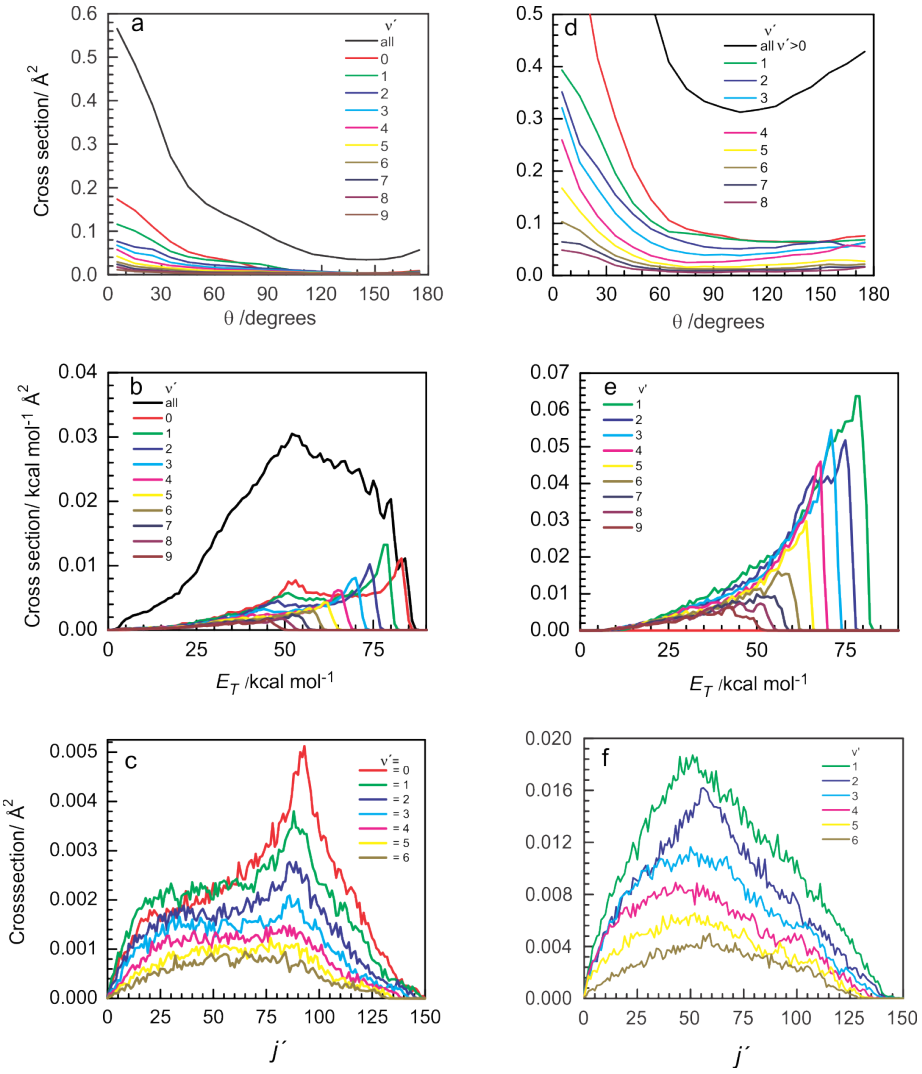

Figure 6. Vibrationally and rotationally resolved distributions of (a-c) reactively scattered $^{16}O^{18}O(v',j')$ molecules and (d-f) inelastically scattered $^{18}O^{18}O$ molecules from collisions of $^{16}O(^3P)$ with $^{18}O^{18}O$ at E_{coll} = 86 kcal mol^{-1}, from QCT calculations. (a,c) Vibrationally resolved angular distributions, $T(\theta)$. (b,e) Vibrationally resolved translational energy distributions, $P(E_T)$. (c,f) Rotational state distributions corresponding to various vibrational states. In (a) and (d), θ is the angle between the scattered $^{16}O^{18}O$ and ^{16}O product, respectively, and the initial direction of the reagent ^{16}O atom in the center-of-mass frame.

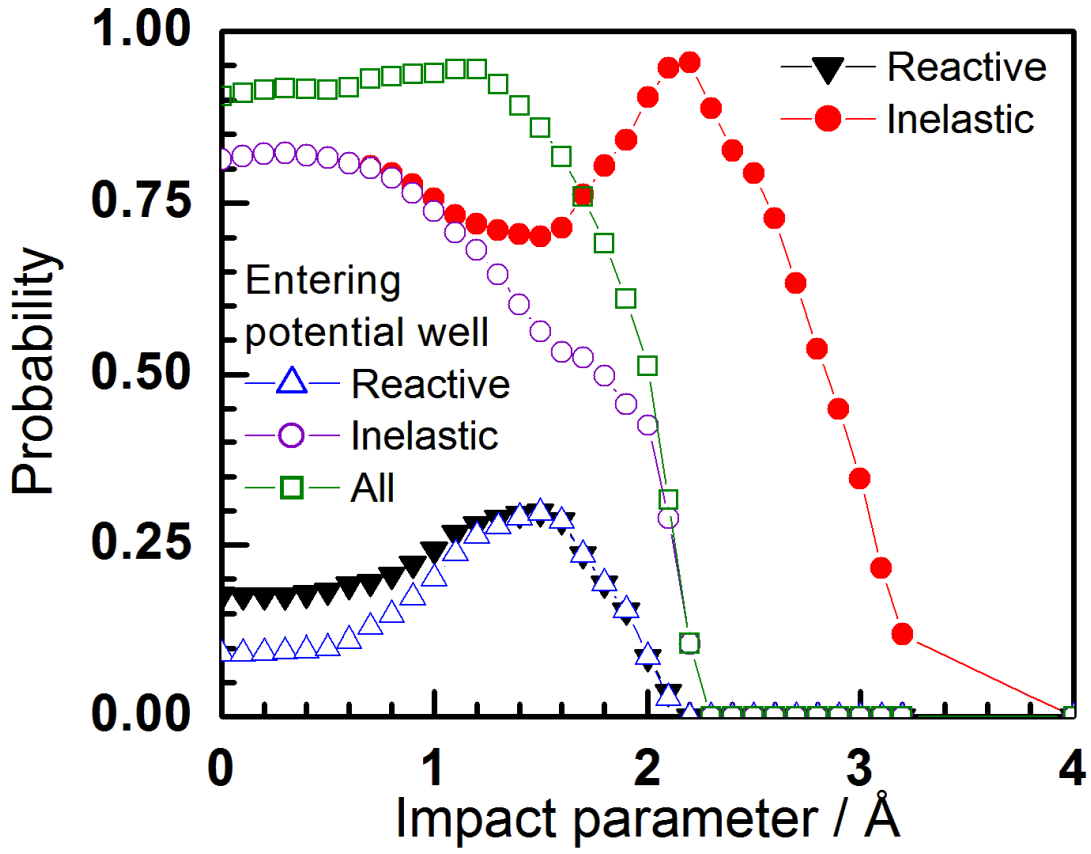

Figure 7. Probability of O-atom exchange ("reaction") and of energy transfer from translation to the internal degrees of freedom of $^{18}O^{18}O$ ("inelastic") as a function of impact parameter, obtained from QCT calculations using the experimental collision energy of 86 kcal mol^{-1}. The probability of entering the potential well in both kinds of collisions is also shown.

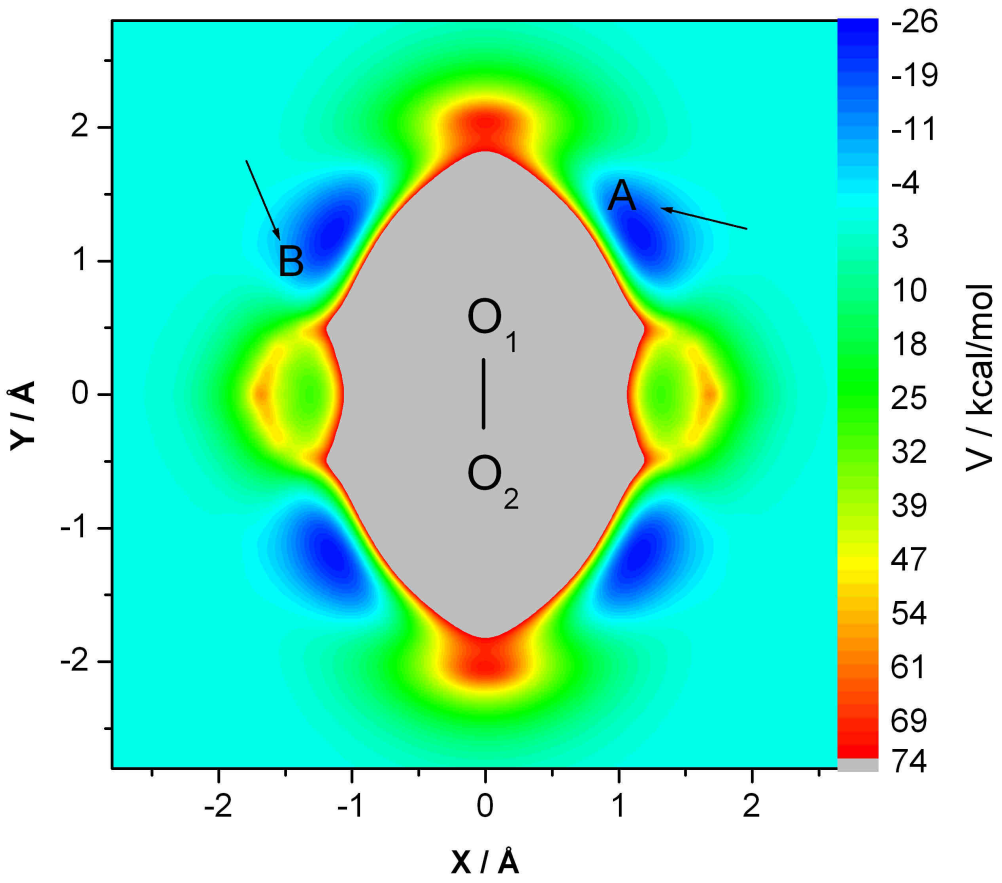

Figure 8. Contour plot of the O + O_2 potential energy surface as a function of the location of the attacking O atom. The O_2 molecule is positioned along the Y axis with its center of mass at the origin of the coordinate system, its bond length being the equilibrium value.

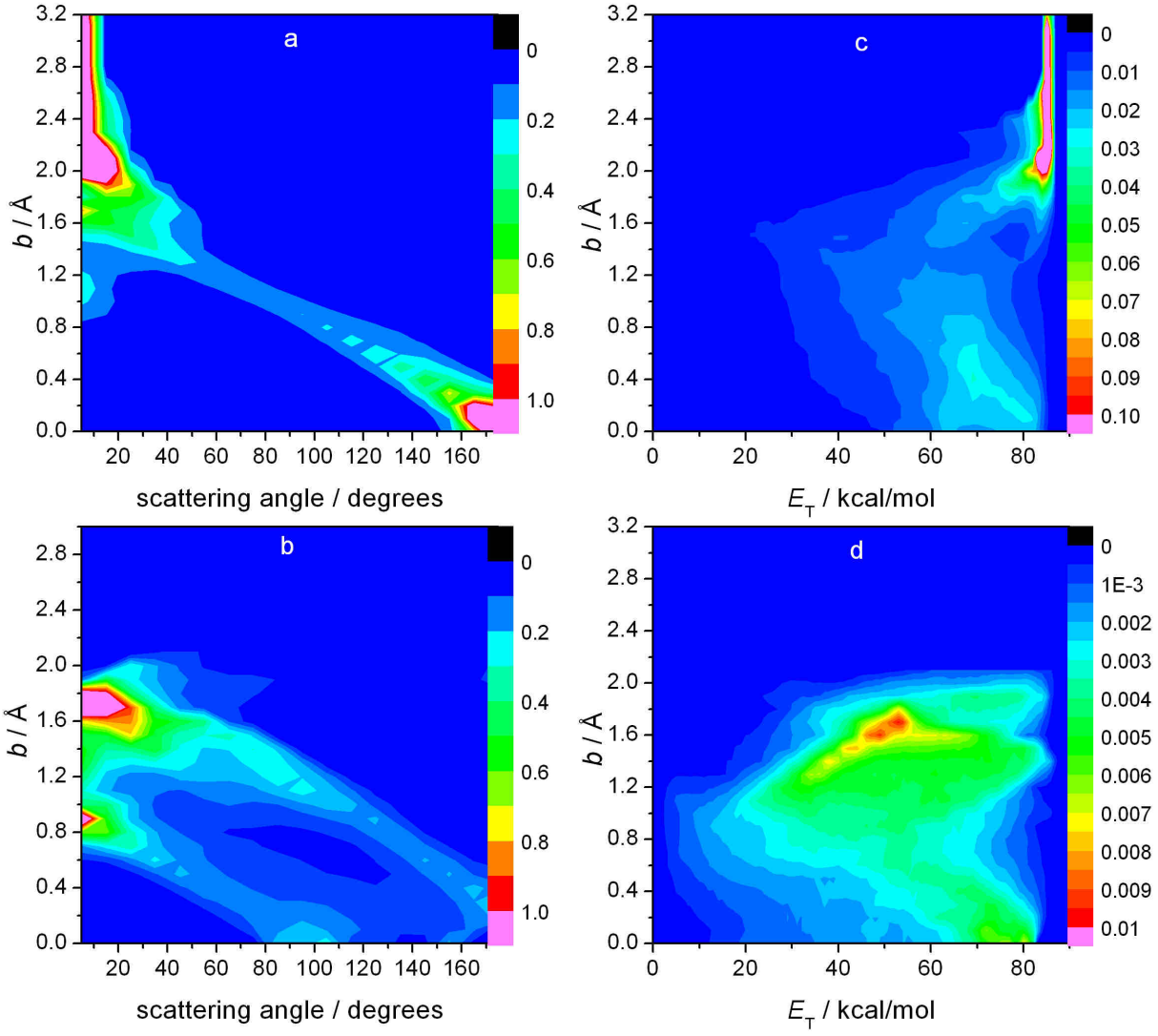

Figure 9. Angular distributions at various impact parameters for (a) inelastic collisions and (b) reactive collisions, and translational energy distributions at various impact parameters for (c) inelastic collisions and (d) reactive collisions. These are QCT results with a collision energy of E_{coll} = 86 kcal mol^{-1}.

Table of Contents Graphic